An elasto-visco-plastic model using the finite element method for crustal and lithospheric deformation

Javier Quinteros [a,b,*], Víctor A. Ramos [a], Pablo M. Jacovkis [b,c]

[a] Lab. of Andean Tectonics, Department of Geological Sciences, FCEN, UBA, Ciudad Universitaria, C1428EGA Buenos Aires, Argentina
[b] Department of Computer Sciences, FCEN, UBA, Ciudad Universitaria, C1428EGA Buenos Aires, Argentina
[c] Faculty of Engineering, UBA, Paseo Colón 850, C1063ACV Buenos Aires, Argentina

ARTICLE INFO

ABSTRACT

A novel numerical model based on solid deformation is presented in this paper. This thermo-mechanical model can simulate the tectonic evolution of crust and (lithospheric and asthenospheric) mantle under different conditions. Our implementation uses the finite element method (FEM) in order to solve the equations. As a Lagrangian approach is employed, remeshing techniques are implemented to avoid distortion problems when a certain deformation threshold is reached. The translation of the state between the old and new mesh is achieved by means of the information stored on Lagrangian particles, which minimizes the diffusion. The model is able to represent elastic, viscous and plastic behaviour inside the studied domain. Three types of creep mechanism (diffusion, dislocation and Peierls) are included. Two different quadrilateral isoparametric elements were implemented and can be employed to perform the calculations. The first one is an element with 4 nodes, selective reduced integration and a stabilization operator to diminish hourglass modes, which reduces the computational time needed. The second one has 8 nodes located in standard positions, uses full integration scheme and has no hourglass modes as it satisfies the Inf-Sup condition. Several test cases with known solutions were run to validate the different aspects of the implementation.

1. Context and purpose of this model

In the last two decades, the development of models to reproduce the processes related to plate tectonics became a powerful tool to achieve a detailed understanding of geodynamics.

On one hand, the deformation and evolution of the uppermost continental crust have been analyzed with satisfactory results by means of a lot of different techniques (see for instance Cristallini and Allmendinger, 2001; Strayer and Suppe, 2002). This type of modelling has an advantage associated with the possibility to compare the results with analog models or field observations.

On the other hand, orogen or regional scale modeling should be constrained with other type of evidence, usually less trustworthy. As analog models are sometimes difficult to scale in order to reproduce the processes that occur at a depth of hundreds of kilometers, where the pressure and temperature conditions play an important role, the numerical approach becomes one of the best options for this type of research.

Many important contributions were developed in the last years in the geodynamic community. Several researchers proposed variations of the model developed by Fullsack (1995) (see for instance Willett, 1999; Pysklywec, 2001; Quinteros et al., 2006; Gerya and Yuen, 2007), which is based mainly on fluid dynamics equations as an analogy to model the behaviour of the crust. However, new models tend to be based on equations that describe the behaviour of solids (Popov et al., 2008). The complexity of these models will be directly related to the number of processes they simulate and the necessary precision in the discretization to capture the solution.

In this paper we present a numerical tool that provides an alternative finite element method optimized to solve new crust–mantle geodynamic problems similar to the approach proposed by Popov et al. (2008). To achieve this, the thermo-mechanical model includes the main laws that describe the deformation of solids in the domain to be modelled. Rheology is considered to be elasto-visco-plastic with three different types of creep mechanism (diffusion, dislocation and Peierls) and Mohr–Coulomb plasticity. Our interest is focused on dynamic deformation occurring on lithosphere, with a special interest in topography evolution and processes that require a good degree of strain localization to be properly simulated. Basically, geodynamic processes that can be simulated in 2D plane strain state.

* Corresponding author at: Deutsches GeoForschungsZentrum GFZ, Telegrafenberg, 14473 Potsdam, Germany. Fax: +49 331 288 1938.
E-mail address: jquinte@dc.uba.ar (J. Quinteros).

The existence of a free stress surface (topography) in the domain was one of the reasons to adopt an Arbitrary-Lagrangian–Eulerian approach (e.g. Fullsack, 1995; Willett, 1999; Pysklywec and Beaumont, 2004 instead of a pure Eulerian one (e.g. Gerya and Yuen, 2003; Braun et al., 2008). A Lagrangian mesh can track the evolution of the domain and handle more consistently boundary conditions applied to parts of the domain that can suffer displacements.

A particle-in-cell method similar to the one implemented by Gerya and Yuen (2007) or Braun et al. (2008) was included. This set of moving particles carries all the necessary information to translate the state of the distorted mesh into a new undeformed one. Here, particles represent material and are not associated with integration points like in the implementation of Moresi et al. (2003).

Some previous models have adopted an explicit scheme (e.g. Babeyko et al., 2002; Gerya and Yuen, 2003; Petrunin and Sobolev, 2006) and, due to this, are restricted in the time step that can apply. This restriction can become important when trying to reproduce long-term deformation over a fine mesh.

We adopt a Backward Euler Method (implicit approach), due to its inherent stability when larger time steps are needed. The resolution of the system of equations is achieved by means of a direct sparse solver. This can impose some limitation when more than ~1 million degrees of freedom are used due to the amount of memory needed at the resolution stage. In cases like this, other techniques that split the resolution into different levels of detail like the Multigrid approach (Moresi et al., 2003) can be more convenient and should be taken into account in the near future. Our code is able to handle complex geometries described by a non-uniform mesh, which makes it suitable to model large domains, with particular emphasis (higher definition) on regions of interest, and track the evolution of interfaces between different types of material. However, at this stage of the development the mesh can be modified to minimize distortion, but the connectivity remains through all the simulation. In comparison, other implementations offer adaptive techniques like Octree (Braun et al., 2008) that are more dynamical but are restricted to cubic representations and lack of a real free surface.

We give details about these features in the next sections.

2. Essentials of the numerical model implemented

Different layers of the lithosphere have very different mechanical behaviour, depending basically on their composition, temperature and pressure conditions. In the upper part of crust, temperature and pressure are relatively low and that is the main reason why the mechanical behaviour is driven by friction and fracture sliding. This type of behaviour is known as "brittle regime" and could be related to plastic behaviour.

In a deeper region, where pressure and temperature are higher, the material has a viscous behaviour, typical of the convective mantle, which is called "ductile regime". Between these regions is located the "brittle–ductile transition", a zone with the highest component of elastic behaviour. This zone is able to store the stress related to its load in order to, for example, produce an isostatic response when the load is reduced or not present anymore.

The numerical model presented is able to predict the thermomechanical behaviour of all the three regimes mentioned, by simulating the response of crust and lithosphere under different conditions such as compression, extension or other cases where only the isostatic compensation is the triggering cause.

2.1. Principal equations

We describe in this section the principal equations and constitutive relationship that were implemented in our code.

The deformation process of compressible material at lithospheric scale can be described by the conservation equations of momentum (Eq. (1)) and thermal energy (Eq. (2)), which can be expressed as

$$\frac{\partial \sigma_{ij}}{\partial x_{ij}} + \rho g = 0 \tag{1}$$

$$\rho C_p \frac{DT}{Dt} = \kappa \nabla^2 T + \rho A - \frac{\partial q_i}{\partial x_i}. \tag{2}$$

Here, σ_{ij} is the Cauchy stress tensor, ρ is density, C_p is heat capacity, κ is thermal conductivity, q is heat flux and D/Dt is the material time derivative.

Radiogenic heating process (A) is included on the right-hand side of Eq. (2). It is known that this modifies the temperature pattern in the upper part of the lithosphere. Also, when the thermal effects appear minor, small temperature variations still affect the viscosity structure. From a mechanical point of view, this fact will inhibit the material to store high levels of stress through the time steps due to the decreasing Maxwell relaxation time (Eq. (9)) and, thus, will retard the arrival to the plastic yield.

A detailed list of symbols and meanings used throughout this text can be seen in Table 1.

We split the stress tensor into its deviatoric and volumetric parts:

$$\sigma_{ij} = \tau_{ij} + P\delta_{ij} \tag{3}$$

where

$$P = \frac{1}{3}\sigma_{ii}. \tag{4}$$

We consider that the deviatoric component of the strain rate can be split into an elastic, a viscous and a plastic component, namely

$$\dot{\varepsilon} = \dot{\varepsilon}^e + \dot{\varepsilon}^v + \dot{\varepsilon}^p = \frac{1}{2G}\hat{\tau} + \frac{1}{2\mu}\tau + \dot{\gamma}\frac{\partial g}{\partial \tau}. \tag{5}$$

where τ is the deviatoric part of the Cauchy stress tensor, G is the shear elastic modulus, μ is viscosity, $\dot{\gamma}$ is the plastic strain rate and g is the plastic potential function.

Table 1
Abbreviations and units.

Symbol	Description	Units
x_i	Coordinates	m
u_i	Displacements	m
T	Temperature	K
t	Time	s
P	Pressure	Pa
Φ	Volumetric strain	
τ_{ij}	Deviatoric stress tensor	Pa
t_M	Maxwell relaxation time	
g	Gravitational acceleration	m s^{-1}
R	Gas universal constant	J mol^{-1} K^{-1}
ρ	Density	kg m^{-3}
K	Bulk modulus	Pa
G	Shear modulus	Pa
B_d	Diffusion creep constant	Pa^{-1} s^{-1}
H_d	Diffusion creep activation enthalpy	J mol^{-1}
B_n	Dislocation creep constant	Pa^{-1} s^{-1}
H_n	Dislocation creep activation enthalpy	J mol^{-1}
n	Dislocation creep exponent	
B_p	Peierls creep constant	s^{-1}
H_p	Peierls creep activation enthalpy	J mol^{-1}
τ_P	Peierls stress	Pa
σ_y	Plastic yield	Pa
σ_0	Cohesion	Pa
θ	Friction angle	°
C_p	Heat capacity	J kg^{-1} K^{-1}
κ	Heat conductivity	W m^{-1} K^{-1}
A	(Radiogenic) heat generation	W kg^{-1}

A stress threshold f is defined as

$$f = \|\tau\| - \sigma_Y(k), \tag{6}$$

where $\|(\cdot)\|$ is the Euclidean norm and k is the accumulated plastic deformation. The plastic flow in this model is assumed to be associative and the plastic potential function is exactly the stress threshold ($g = f$). In case of plasticity $f = 0$.

The volumetric part is considered to be always purely elastic and the pressure can be expressed as

$$P = K\Phi, \tag{7}$$

where K is the bulk elastic modulus and Φ is the volume change.

Finally, the volumetric deformations are followed by corrections in the calculation of density, namely

$$\rho = \rho_0 \left[1 + \frac{P}{K}\right]. \tag{8}$$

The Maxwell relaxation time is defined as

$$t_m = \frac{\mu}{G} \tag{9}$$

and the viscous stress relaxation coefficient since the last time step is

$$\alpha = \frac{1}{1 + (\Delta t / t_m)}, \tag{10}$$

where Δt is the time step.

Also, the effective visco-elastic modulus is defined as

$$G^{ve} = \alpha G. \tag{11}$$

To be consistent with the *brittle regime*, the shear stress at any point cannot exceed the maximum shear stress as a function of depth (σ_y) calculated by Byerlee (1978). This is expressed as

$$\sigma_y = \sigma_0 + \frac{\Phi - 1}{\Phi}\rho gz, \tag{12}$$

where σ_0 is the cohesion strength, $\Phi - 1/\Phi$ is the friction coefficient,

$$\Phi = \left[(1 + \eta^2)^{1/2 - \eta}\right]^{-2} \tag{13}$$

and

$$\eta = \tan(\theta), \tag{14}$$

where θ denotes the considered friction internal angle.

2.2. Material rheology

Numerous researchers have studied the behaviour of the rocks under different pressure and temperature conditions (see for instance Jaoul et al., 1984; Mackwell et al., 1998). The viscosity is usually considered to be dependant on many variables; particularly, on the creep constants (e.g. B_d, B_n), strain rate ($\dot\varepsilon$), temperature (T), activation coefficient (e.g. E_d, E_n) and a power law exponent (n), among others.

Three different types of creep are included in the definition of rheology employed in this model, following the approach of Kameyama et al. (1999), in a similar way as it was implemented in Sobolev and Babeyko (2005) and in Popov et al. (2008). These are the three competing creep mechanisms that are usually related to olivine: diffusion, dislocation and Peierls creep. In this approach, at a given temperature and stress, the mechanism that produces the highest viscous strain rate becomes the dominant creep mechanism (Babeyko et al., 2006). It should be noted that many codes do not include the Peierls mechanism, which can lead to some differences in the viscosity calculation when temperature is low and differential stress is high, as it is shown in Popov et al. (2008).

Effective viscous strain rate is additively decomposed into these three mechanisms, namely

$$\dot\varepsilon_{\text{eff}}^{(v)} = \dot\varepsilon_d + \dot\varepsilon_n + \dot\varepsilon_p. \tag{15}$$

Strain rate due to diffusion creep is defined as

$$\dot\varepsilon_d = B_d \tau_{II} e^{-H_d/RT}, \tag{16}$$

dislocation, power-law creep as

$$\dot\varepsilon_n = B_n \tau_{II}^n e^{-H_n/RT}, \tag{17}$$

and Peierls creep as

$$\dot\varepsilon_p = B_p e^{[-H_p/RT(1 - (\tau_{II}/\tau_p))^q]}, \tag{18}$$

where τ_{II} is the square root of the second invariant of the stress tensor, R is the gas constant, B_d, B_n, B_p are creep parameters, H_d, H_n, H_p are activation enthalpies for each creep and τ_p is Peierls stress.

Later, effective viscosity is calculated as

$$\mu = \frac{\tau_{II}}{2\dot\varepsilon_{\text{eff}}^{(v)}}. \tag{19}$$

Some of these creep mechanisms can be omitted for specific definitions of input parameters (e.g. B_p and B_d).

3. Finite element discretization

To apply the finite element method, two different two-dimensional, quadrilateral elements were implemented. In the first place, an element with 4 nodes (NN = 4) proposed by Liu et al. (1994). This element uses selective reduced integration to avoid the volumetric and shear locking and to reduce the computational time needed. To perform some sort of control over the *hourglass modes*, it defines a stabilization operator by means of the partial derivatives of the generalized strain rate vector related to the natural coordinates.

Shape functions (h) are defined as usual for a quadrilateral element with 4 nodes. Spatial coordinates (x) and also primary variables are approximated by the following linear combinations

$$x_i = \sum_{a=1}^{NN} h_a(r, s) x_{ia} \tag{20}$$

and

$$v_i = \sum_{a=1}^{NN} h_a(r, s) v_{ia}, \tag{21}$$

where subindex i represents the dimension and a is the element number.

The strain rate is expressed as

$$\dot\varepsilon(r, s) = \sum_{a=1}^{NN} B_a(r, s) v_a, \tag{22}$$

where B_a is the gradient matrix that contains the shape functions derivatives.

If $\dot\varepsilon$ is expanded in a Taylor series that is centered on the element natural coordinates (0,0)

$$\dot\varepsilon(r, s) = \dot\varepsilon(0, 0) + \dot\varepsilon_{,r}(0, 0)r + \dot\varepsilon_{,s}(0, 0)s, \tag{23}$$

it can be approximated by

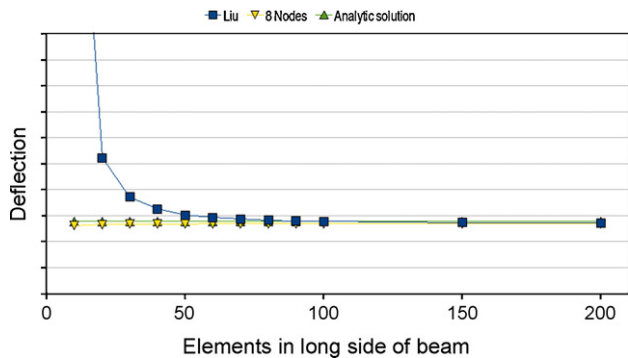$$\dot\varepsilon(r, s) = \sum_{a=1}^{NN} \bar{B}_a(r, s) v_a, \tag{24}$$

Fig. 1. Convergence of the Liu element (4 nodes) and the standard 8 nodes element as a function of the number of elements on the long side of the beam.

where

$$\bar{B}_a(r, s) = B_a(0, 0) + B_{a,r}(0, 0)r + B_{a,s}(0, 0)s. \tag{25}$$

To diminish the volumetric locking, selective reduced integration is applied (Hughes, 1980). $\bar{B}_a(r, s)$ is split into its deviatoric and volumetric part

$$\bar{B}_a(r, s) = \bar{B}_a^{vol}(0, 0) + \bar{B}_a^{dev}(r, s). \tag{26}$$

The volumetric part of the matrix is evaluated only at point (0,0) to avoid volumetric locking. $\bar{B}_a^{dev}$ can be expanded as in Eq. (25), namely

$$\bar{B}_a(r, s) = B_a(0, 0) + B_{a,r}^{dev}(0, 0)r + B_{a,s}^{dev}(0, 0), \tag{27}$$

where $B_a(0, 0)$ is the gradient matrix evaluated at (0,0) with both volumetric and deviatoric parts.

The elemental formulation asserts the diminishing of the volumetric locking, even if it is integrated at just one Gauss point. However, this is usually not enough in the case in which a plastic deformation front should be accurately detected in an elasto-plastic problem. That is the main reason to integrate at two Gauss points:

$$\text{Point1} : \left(+\frac{1}{\sqrt{3}}, +\frac{1}{\sqrt{3}} \right); \quad \text{Point2} : \left(-\frac{1}{\sqrt{3}}, -\frac{1}{\sqrt{3}} \right). \tag{28}$$

Liu et al. (1994) claim that no hourglass mode should be present, but this effect could arise under particular boundary conditions and after many time steps, particularly in boundaries with high pressure (e.g. bottom boundary) that are subject to pressure boundary conditions (e.g. Winkler) that allow the displacement in both coordinates.

Even when we did not face this problem, we also tested successfully a standard quadrilateral element with 9 nodes and normal Gauss integration. The main drawback of this element is the increase in the computational time needed. However, when the mesh is fine enough, the results showed no substantial differences. This would give the chance to select the element that presents more benefits for the type of problem that needs to be solved.

The main reason to adopt the 4-noded element would be the computational time. Basically, as the number of nodes per element is smaller, the total size of the system of equations would be considerably reduced. Also, as it integrates only at two Gauss points, instead of nine in the other case, the calculations would become faster.

On the other hand, one can see in Fig. 1 the results of convergence for a cantilever beam benchmark case similar to the one presented in the next section. It is clear that with a proper definition of the mesh both results should converge to the solution, but the convergence rate of the 4-noded element is not so fast as the other one.

Other codes use different techniques to treat or avoid this type of collateral effects. Gerya and Yuen (2003, 2007) use a staggered finite differences method that is known to be inherently stable. However, we consider that due to its pure Eulerian approach it would not be the best choice for the treatment of free surface.

Moresi et al. (2003) apply some sort of average or diffusion to the variables in order to avoid the *checkerboard pressure* distribution (Bathe, 1996), problem that can be considered similar to the hourglass modes.

Popov et al. (2008) employ differential density to reduce the effects of *hourglass* and complement this with intensive use of remeshing.

3.1. Stress update algorithm

As a Lagrangian approach was adopted for the transient problem, an algorithm published by Hughes and Winget (1980) was implemented to take into account the finite rotations of the material in the stress update algorithm. By this, the gradient G is defined as

$$G_{ij} = \frac{\partial \delta_i}{\partial y_j^{n+1/2}} \tag{29}$$

and strain (γ) and rotation increments (ω) can be defined in terms of G:

$$\gamma = \frac{G + G^T}{2}, \tag{30}$$

$$\omega = \frac{G - G^T}{2}. \tag{31}$$

The following definition is proposed for integrating the constitutive equation:

$$\tau^{n+1} = \bar{\tau}^{n+1} + \Delta\tau \tag{32}$$

where

$$\bar{\tau}^{n+1} = Q\tau^n Q^T, \tag{33}$$

$$Q = \left(I - \frac{\omega}{2} \right)^{-1} \left(I + \frac{\omega}{2} \right), \tag{34}$$

τ^n is the unrotated deviatoric stress from the previous timestep, I is the identity matrix and $\Delta\tau$ is the stress increment.

A prediction–correction stress update algorithm was adopted to properly calculate stress over discrete time steps considering the elasto-visco-plastic behaviour. It can be expressed by means of

$$\tau_{n+1} = 2G^{ve}\Delta\varepsilon_{n+1} + \alpha\tau_n - 2G^{ve}\Delta\gamma_{n+1}n_{n+1}, \tag{35}$$

where τ_{n+1} is the deviatoric stress at the $(n + 1)$-th time step, $\Delta\varepsilon_{n+1}$ is the strain increment at the $(n + 1)$-th time step and $\Delta\gamma_{n+1}$ is the effective plastic strain increment at the $(n + 1)$-th time step, which is defined as

$$\Delta\gamma_{n+1} = \frac{\|\tau_{n+1}^{pr} - \sigma_y\|}{2G^{ve}}, \tag{36}$$

and where predicted visco-elastic stress is

$$\tau_{n+1}^{pr} = 2G^{ve}\Delta\varepsilon_{n+1} + \alpha\tau_n. \tag{37}$$

As the problem is non-linear, a classical Newton–Raphson iteration is performed. To achieve a high convergence rate of this algorithm, an appropriate stress update algorithm linearization is fundamental. In this model, a consistent tangential operator proposed by Simo and Taylor (1985) is employed.

This is defined as

$$C_{ijkl}^{tg} = K\delta_{ij}\delta_{kl} + A \left[\frac{1}{2} \left(\delta_{ik}\delta_{jl} + \delta_{il}\delta_{jk} \right) - \frac{1}{3}\delta_{ij}\delta_{kl} \right]$$
$$- B \left(n_{n+1}^{pr} \right)_{ij} \left(n_{n+1}^{pr} \right)_{kl}, \tag{38}$$

where

$$A = 2G^{ve}\left(1 - \frac{G^{ve}\Delta\gamma_{n+1}}{\|\tau_{n+1}^{pr}\|}\right). \tag{39}$$

$$B = 2G^{ve}\left(\frac{G^{ve}}{G^*} - \frac{G^{ve}\Delta\gamma_{n+1}}{\|\tau_{n+1}^{pr}\|}\right). \tag{40}$$

3.2. Discretization of heat transport equation

As in the mechanical part, an implicit approach is adopted for the system of equations related to conservation of energy. Newton–Raphson iterations are applied to solve the non-linearities related to this equation. The variable is not the temperature (T), but the temperature increment (ΔT). Then, temperature is split in the following way:

$$^{t+\Delta t}T^{(i)} = {}^{t+\Delta t}T^{(i-1)} + \Delta T, \tag{41}$$

where the superscript to the left represents the particular time when the variable is considered and the superscript to the right the iteration number for the present time step.

Starting from the principle of virtual temperatures (Bathe, 1996),

$$\int_V \bar{T}^T {}^{t+\Delta t}(\rho C_p)^{t+\Delta t}\dot{T}\partial V + \int_V \bar{T}'^T {}^{t+\Delta t}k^{t+\Delta t}\dot{T}'\partial V$$
$$= \int_V \bar{T}^T {}^{t+\Delta t}q^B \partial V + \int_{S_q} \bar{T}^S {}^{t+\Delta t}q^S \partial S_q, \tag{42}$$

and after some algebraic steps, the following expression can be obtained:

$$\left[\int_V B^T \kappa B \partial V + \int_V H^T \frac{\rho C_p}{\Delta t} H \partial V\right]\Delta T =$$
$$\left[\int_V H^T A - B^T \kappa B^{t+\Delta t}T^{(i-1)} - H^T \frac{\rho C_p}{\Delta t}H\left({}^{t+\Delta t}T^{(i-1)} - {}^t T\right)\partial V + \int_{S_q} H^{S_q T}q^{S_q}\partial S_q\right], \tag{43}$$

where H is the one-dimensional interpolating matrix that contains the isoparametric shape functions, B is the gradient matrix related to the same shape functions, q^{S_q} is the thermal flux imposed on boundary S_q and ${}^t T$ is the already converged solution of the previous time step.

As part of the coupling between thermal and mechanical parts of our code, advection of temperature is taken into account by the displacements resulting from the mechanical model. This approach was already used in other numerical codes (e.g. Babeyko et al., 2002; Sobolev and Babeyko, 2005).

4. Solution scheme

The resolution of one time step is accomplished by a Newton–Raphson iteration, which is outlined in the following steps.

(1) Apply Newton–Raphson iterations in order to reach a solution for the non-linear problem.
  (a) Include result of previous iteration of the current time step by means of updated Lagrangian formulation (Bathe, 1996).
  (b) Assemble stiffness matrices and external force vectors related to Eqs. (1) and (2) and solve both linearized systems (mechanical and thermal).
  (c) Update temperature and displacements on the nodes.
  (d) Check convergence and return to step 1 if necessary.

(2) Add increments of secondary variables (e.g. stress, plastic strain) to Lagrangian particles.
(3) Advect particles interpolating displacements.
(4) Move nodes according to calculated displacements.
(5) If deformation of the mesh is above a certain threshold, remeshing is needed (see Section 4.1).

(a) Build (or recover) the stiffness matrix of a Laplace equation associated with the geometrical coordinates of the nodes.
(b) Apply Dirichlet boundary conditions to the nodes that must be kept fixed in space. Usually, nodes located over the boundary of the domain and the ones that track important interfaces.
(c) Check new position of the particles relative to the new mesh, namely, inside which element the particles are located and their elemental coordinates.
(d) Keep particles per element in accordance to a predefined range.
(e) Map properties stored in the particles to the new mesh.

Details of the different steps mentioned in the previous scheme are given in the following sections.

4.1. Remeshing procedure

In a Lagrangian formulation, the mesh is distorted every time step due to the deformation of the studied body. When the body accumulates too much deformation in a few elements, numerical issues may arise.

The main problem when calculating on a distorted mesh is the slow (or absence of) convergence. In this case, a new mesh with minimum deformation should be generated. When boundaries are fixed and deformation is concentrated inside the body, the new mesh could be exactly the original one. This solution is optimum because it requires no computational time. However, this is not the general case in Lagrangian approaches to geological problems, where at least the boundary representing the topography is a stress free surface and will move apart from its original position.

The position of the nodes in the boundary defines the domain; thus, these are considered to be *fixed* during the remeshing process. The internal nodes should be relocated in such a way that the elements are preferably not deformed.

A maximum deformation threshold is defined, which is compared with the accumulated deformation of elements at every time step. When the deformation for any element is above this threshold, the domain is remeshed.

A simple mesh is considered (e.g. the original mesh) and an appropriate mapping is defined to adapt it to the arbitrary positions of the boundary ($\partial\Omega$) nodes. The problem can be stated as a Laplace equation for each coordinate (x and y)

$$\Delta\phi = 0 \text{ in } \Omega. \tag{44}$$

constrained by the Dirichlet conditions by which $\phi = x$ at $\partial\Omega$ and $\phi = y$ at $\partial\Omega$ (Carey and Oden, 1984).

A stiffness matrix (K) related to the Laplace equation is assembled with the original undeformed mesh. Later, when the deformation threshold is reached, Dirichlet conditions are applied based on the present positions of the boundary nodes. Finally, both system of equations are solved once for each coordinate (x and y) and the nodes position is updated according to this result.

Depending on the type of problem, less Dirichlet boundary conditions can be defined. When the displacement of the material generates a non-uniform distribution of nodes at specific parts of a boundary, some Dirichlet conditions can be discarded to have again a uniform distribution.

One can see in Fig. 2a and b how the node in the middle is shifted to the rightmost part of the bottom boundary. When remeshing is applied the deformation of the elements is distributed
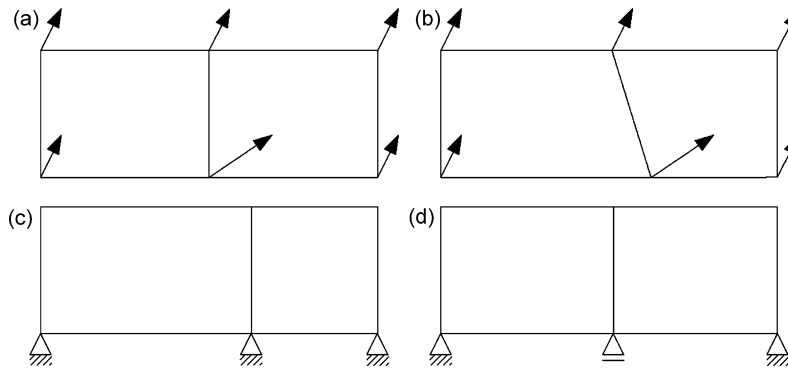
Fig. 2. (a) Subset of elements next to a boundary and the displacements for a given time step. (b) Distorted mesh where the nodes tend to concentrate on the rightmost corner. (c) Even when the distortion of the elements in the inner part of the domain is solved by the Laplace equation, an anomalous distribution of nodes over the boundary leads to a poor mesh quality. (d) If domain definition is not substantially changed, Dirichlet conditions for one of the coordinates can be discarded in order to properly redistribute the boundary nodes.

by means of the Laplace equation and the quality of the mesh inside the domain improves. However, the width of the elements will not be uniform and they will tend to concentrate to the right (Fig. 2c).

A solution to avoid this situation is to discard the Dirichlet conditions related to the x position of the nodes over the bottom boundary. Thus, the width of the elements will have exactly the same proportion among them as in the original mesh. In this case, the only 2 nodes of this boundary whose x coordinate should be set as Dirichlet conditions are the leftmost and the rightmost (Fig. 2d).

4.2. State mapping or translation

The next step following the creation of a new mesh is the state mapping. All the variables that describe the state of the domain at a certain time step are associated with nodes and elements of the old mesh, a situation that is not valid in the new mesh. To deal with this problem, particles carrying information about all the variables that describe the domain state are incorporated. The state is reproduced by translating the information stored in the particles to each node and element of the new mesh (e.g. Harlow and Welch, 1965; Gerya and Yuen, 2003).

The position of these particles is updated at every time step based on the displacements calculated by the finite element model. The shape functions h_n are evaluated at the particle position and multiplied by the nodal displacements. For example, in a four node element we can write

$$u_{i,p} = \sum_{n=1}^{4} h_n(r, s).u_{i,n}, \tag{45}$$

where u is the displacement, i is the coordinate, n is the node number and q is the particle.

In the distorted mesh, each particle stores the information about the element to which it belongs. As in the new mesh, the element that contains the particle must be found, the old element is probably the best starting point to look for. A modified algorithm based on the one proposed by Novoselov et al. (2002) was implemented. This way, the order of the search is considerably reduced.

To verify whether the particle belongs to a certain element, the following steps are accomplished.

(1) The quadrilateral is split into two triangles. The first one is the one where $s > r$ and the second one is its complement ($r > s$).
(2) A simple geometrical relation using the coordinates of the corner nodes $(n_x^1, n_y^1, n_x^2, \ldots)$ is employed to check whether the particle belongs to the first triangle. Namely,

$$\begin{bmatrix} a_1 \\ a_2 \\ a_3 \end{bmatrix} = \begin{bmatrix} n_x^1 & n_y^1 & 1 \\ n_x^2 & n_y^2 & 1 \\ n_x^3 & n_y^3 & 1 \end{bmatrix}^{-1} \cdot \begin{bmatrix} 1 \\ -1 \\ -1 \end{bmatrix} \tag{46}$$

and

$$\begin{bmatrix} b_1 \\ b_2 \\ b_3 \end{bmatrix} = \begin{bmatrix} n_x^1 & n_y^1 & 1 \\ n_x^2 & n_y^2 & 1 \\ n_x^3 & n_y^3 & 1 \end{bmatrix}^{-1} \cdot \begin{bmatrix} 1 \\ 1 \\ -1 \end{bmatrix}, \tag{47}$$

r and s being the elemental coordinates calculated as

$$r = a_1 m_x + a_2 m_y + a_3 \quad \text{and} \quad s = b_1 m_x + b_2 m_y + b_3 \tag{48}$$

(3) The particle is considered to be inside the first triangle if

$$|r| <= 1 \quad \text{and} \quad |s| <= 1 \quad \text{and} \quad r < s \tag{49}$$
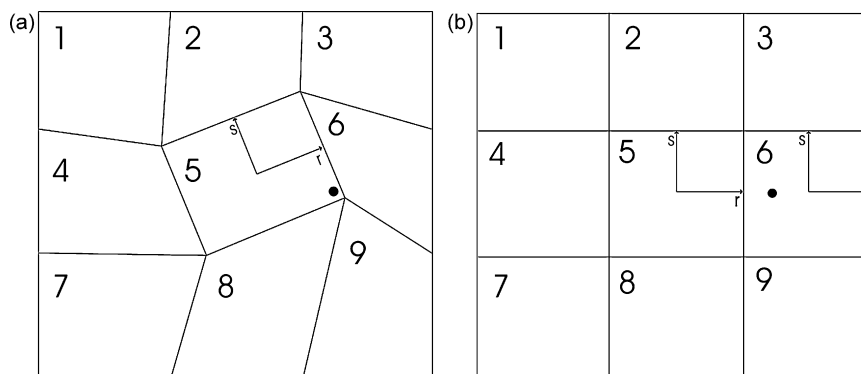

Fig. 3. Particle position before and after the remeshing process. (a) Inside element 5 in the distorted mesh. (b) Inside element 6 in the new undistorted mesh.
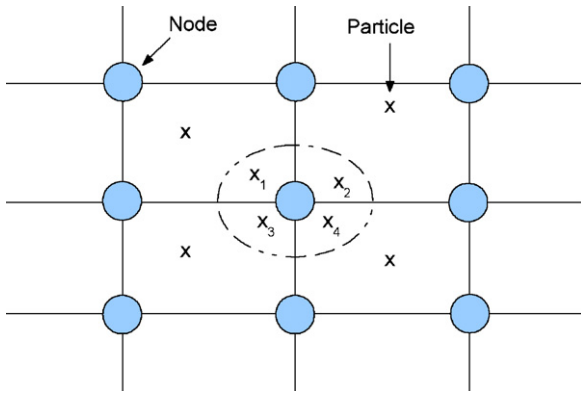
Fig. 4. Schematic view of the state setting in the nodes after remeshing. The closest particle from each adjacent element is selected and the average is assigned to the node.

(4) Analogous operations are performed for the second triangle.
(5) If the local coordinates of the particle are outside the element, the search algorithm uses the calculated coordinates (r and s) to decide in which direction should search further and goes back to 1.

We show in Fig. 3a the position of a particle which, before the remeshing, belonged to element number 5. After remeshing, the new local coordinates related to element number 5 are calculated and, in this case, the variable r does not satisfy Eq. (49) (see Fig. 3b). Then, the neighbour element that shares the side associated with $r = 1$ condition is searched. This search requires a low computational cost due to the connectivity list of nodes and elements.

It is quite difficult for the particle to be located far from the former element. To be stricter, there is a small probability that the new element is relocated far from its original position. A situation like this could happen if the mesh had suffered a great deformation, which is not probable considering the convergence needed. So, the number of particles that must be relocated at a distance greater than a few elements (compared to the total amount of elements) is completely marginal.

Once the new relation between particles and elements is calculated, the state of the domain must be translated to the new mesh. For every node, one particle from each element to whom it belongs is selected and an average of its properties is calculated and assigned to it (Fig. 4).

The number of particles inside an element may vary due to this relocation. As the domain state in the new mesh is replicated exclusively by the particles, the number of particles inside an element must exceed a defined minimum threshold. To avoid this problematic situation, a new set of particles is inserted if an element contains less particles than the minimum threshold. The variables of the new particles are calculated based on the values of the existing ones.

Fig. 5 shows an example of the remeshing process and the mapping of a variable. There, the stress and the mesh configuration at the time step when the remeshing is applied and one time step later can be seen.

5. Computational aspects

The numerical model was completely implemented in C++ using object-oriented programming techniques. It is based on a more general-purpose framework (Quinteros et al., 2007) designed to solve problems related to partial differential equations by means of the finite element method.

In domains where fine resolution is needed, the most time-consuming stage is the resolution of the set of algebraic equations, related to the discretization produced by the finite element method. To solve this system of equations, we use in our code a direct solver capable of handling large sparse matrices. Our election is based on the robustness of this type of solvers when matrices are ill-conditioned, a common situation in highly non-linear problems.

Actually, different direct solvers were easily linked to our code due to the decoupling between the high-level model implementation and the low-level calls to the solver, by means of Object-Oriented Programming. The results provided in this paper were obtained with Pardiso (Schenk et al., 2001), which has a good performance on multi-processor (or multi-core) computers.

Although this remark is beyond the scope of this paper, we would like to point out that the code was also run on a cluster environment with MUMPS solver (MUltifrontal Massively Parallel Sparse direct solver) (Amestoy et al., 2000) including METIS ordering (Karypis and Kumar, 1999) in order to improve the quality of the matrix. Then, the resolution of equations is calculated in parallel using standard MPI protocol and using the resources on all the nodes in the cluster and not only on a multi-core computer.

It should be noted that both of these solvers provide a first step towards the parallelization of the final code, at least on the resolution stage. Also, in both cases part of their good performance is related to the extensive use of scalar and algebraic functions
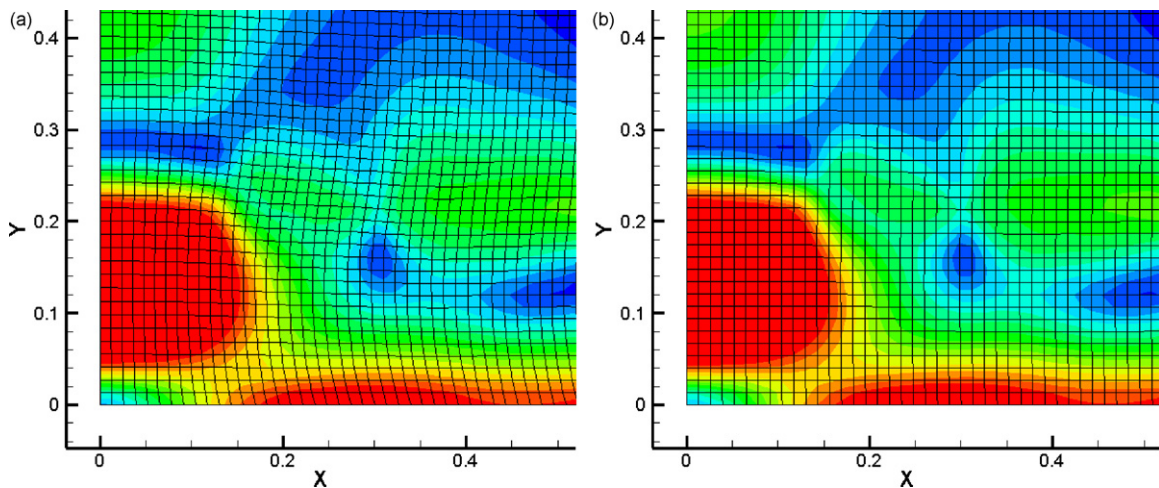

Fig. 5. Deviatoric stress state and mesh geometry in two consecutive time steps: (a) before and (b) after the remeshing.
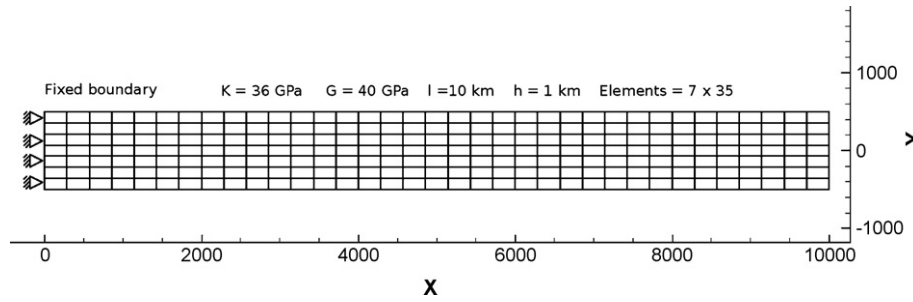
Fig. 6. Setup of the cantilever beam test case. Initial configuration of the elastic cantilever beam and material properties. No external forces act over the beam. Bending is driven only by gravity force. Values similar to the ones used in geodynamical problems were selected for material properties and load. Here, K and G are bulk and shear moduli and l and h are width and height of the beam.

implemented on other packages like BLAS I/II/III (Dongarra, 2002) or SCALAPACK (Blackford et al., 1997).

Our implementation was thoroughly tested in order to include as many optimizations as possible and to avoid memory leaks that could compromise the simulation of large domains during many time steps.

As an implicit approach is used, the stiffness matrix must be constructed at every single iteration. The computational cost of this operation is drastically reduced by creating the structure of the stiffness matrix when the mesh is first created and keeping not only the structure but also, if the solver supports this feature, the first stage of factorization, which is related to the distribution of non-zero values and their magnitudes. Neither of these will change considerably through iterations of the same time step nor even from one time step to another, as long as the same mesh is used. When a certain level of distortion is reached, the mesh – and the structure of the stiffness matrix – are created again.

6. Code validation

To validate the formulation and implementation of the model, a series of test cases with known results were run. In the following subsections, details are given about some of the cases that validate each behaviour mode simulated (elastic, viscous and plastic).

The elasticity test was run with the standard quadrilateral element with 8 nodes that showed a better convergence rate compared to the element proposed by Liu (Fig. 1). In the other two cases, quality of discretization needed to solve the problem was enough to get a good solution with the Liu element and, therefore, this was used to optimize computational time.

6.1. Clamped beam—Elasticity

The bending of a cantilever elastic beam is a common test case to validate the proper calculation of elastic behaviour. There is an

analytical solution not only for the maximum deflection, but also for the bending stress.

In this case, a two-dimensional model of an elastic beam in plane strain state is considered. The beam is fixed on its left side and bends due to gravity. No external force is applied on it, only body forces associated with its own weight. The general setup of the model can be seen in Fig. 6 and the parameters and properties of the material are listed in Table 2.

Dimensions were selected to provide a test closer to the figures that are common in geodynamics. Size of the beam is in the order of magnitude of crust and density was considered to be approximately one order of magnitude lower than crustal values, because that is the usual difference between load and restoring forces.

Under the Euler–Bernoulli approximation, maximum deflection of this elastic beam can be expressed as

$$w = \frac{3\rho g l^4}{2Eh^2}, \tag{50}$$

where ρ is density, g is gravity constant, l is the length of the beam and E is the Young's modulus of the material, which can be calculated from the bulk (K) and shear (G) moduli by means of the following expressions:

$$E = 2G(1 + \nu), \tag{51}$$

$$\nu = \frac{3K - 2G}{6K + 2G}. \tag{52}$$

Bending stress can also be expressed as a function of material properties, namely

$$\sigma_b = \frac{3\rho g l^2}{h} \tag{53}$$

The size of the beam is long enough to be considered *thin*, a necessary condition to use the Euler–Bernoulli theory.

One can see in Fig. 7 the calculated shape of the beam after deflection and a colour plot of the distribution of bending stresses. Also, the maximum values of deflection and stress are shown. To compare the analytical and numerical solutions, the height of the beam was slightly reduced to match the location of integration points. It can be seen in Table 2 that results are quite accurate even for a coarse definition of the mesh.

An evolution of the convergence of discretization due to refinement of the mesh can be seen in Fig. 8. The number of elements used for the vertical discretization of the beam is plotted against the relative error of the calculation. It can be appreciated in the figure that displacements and also stresses converge to the analytical solution very fast. The aspect ratio of the elements used was the same throughout all the experiments to discard the possibility of inaccuracies produced by distortion of the elements.
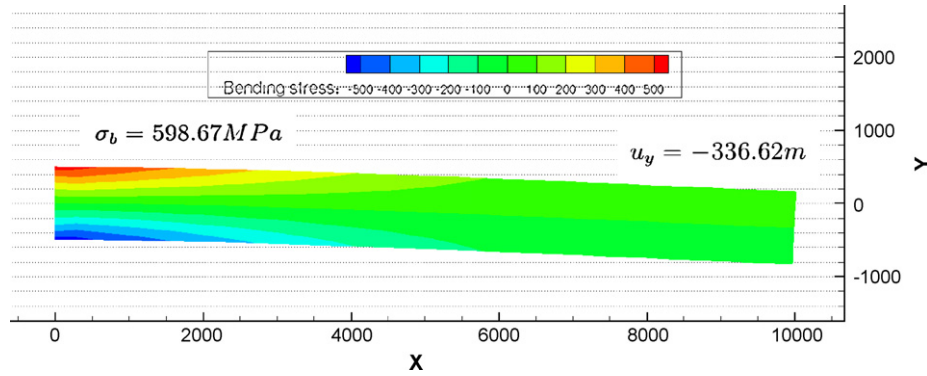
Table 2
Parameters used for the cantilever beam benchmark. Results compared to the analytical solutions are shown in the second part of the table.

Variable	Description	Value
K	Bulk modulus	36 GPa
G	Shear modulus	40 GPa
ρ	Density	200 kg m^{-3}
l	Length of the beam	10 km
h	Height of the beam	1 km
$n_l x n_h$	Number of elements	35 × 7
w_{an}	Analytical deflection	336.62 m
w_{num}	Numerical deflection	335.88 m
err_w	Relative deflection error	0.2%
σ_{an}	Analytical bending stress	598.67 MPa
σ_{num}	Numerical bending stress	590.5 MPa
err_σ	Relative stress error	1.3%

Fig. 7. Shape of the elastic cantilever beam after bending. Values for maximum vertical displacement (u_y) and bending stress (σ^{max}) are shown above the beam. Stress distribution is also shown by means of a contour plot.
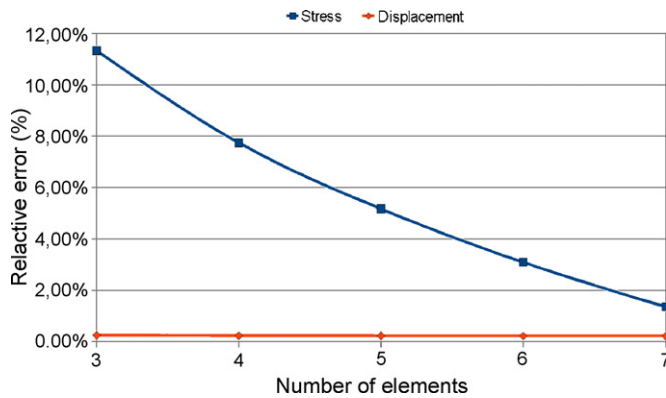

Fig. 8. Relative error of stresses and displacements compared to the number of elements across the elastic plate thickness.

6.2. Rayleigh–Taylor instability—Viscosity

The test case proposed by van Keken et al. (1997) was selected to validate the viscous behaviour. In this test, the evolution of a two phase fluid that convects induced by gravity is tracked. The domain has bottom and upper boundaries of 0.9241 m and left and right boundaries of 1 m. The two phases of the fluid have the same viscosity but different density ($\Delta\rho$). The lighter fluid (fluid 1) is on the bottom part of the domain and the denser one (fluid 2) is above. The limit between both fluids is located at 0.2 m from the bottom and with an initial deflection described by the expression

$$w = 0.02 \cos\left(\frac{\pi x}{\lambda}\right), \tag{54}$$

where λ is the width of the domain. A schematic view of the domain and the boundary conditions is shown in Fig. 9.

The specification of both fluids can be seen in Table 3.

Over the upper and bottom boundaries *non-slip* conditions are prescribed. Over the lateral walls vertical displacements are allowed but not horizontal ones (symmetric conditions). This way, the motion is strictly gravity driven. Gravity is considered to be 1 ms^{-2}.

Table 3
Main features of the fluids from the isoviscous Rayleigh–Taylor instability problem.

Variable	Fluid 1	Fluid 2
Density (ρ)	1.3	1.0
Viscosity (μ)	1	1
Elastic Bulk modulus (K)	1000	1000
Elastic Shear modulus (G)	1000	1000
Cohesion strength (σ_0)	∞	∞
Gravity (g)	1	1

The evolution in time of the fluid can be seen in Fig. 10.

Different snapshots from the domain evolution that are shown in Fig. 10 were compared with the ones published by van Keken et al. (1997). The evolution shown in this chapter and in the van Keken paper are identical for all the compared time steps. The only minor difference that could be found is located over the contact between both fluids near the bottom. This difference is explained by the uniform discretization performed prior to the simulation, which does not match exactly the one proposed in Eq. 54. It is very important to note that, due to the intense deformation that this case implies, not only the capability of the model to represent viscous behaviour is validated, but also the implementation of the remeshing algorithm.

6.3. Plastic deformation concentration—Plasticity

One of the aims when modelling plastic behaviour is to have a good localization of the plastic deformation. This means that the concentration of the plastic deformation when simulating fractures should not be wider than a few elements.

In this case, an isotropic solid is compressed. The setup of the experiment consists of a 3 m high and 10 m wide block, with the
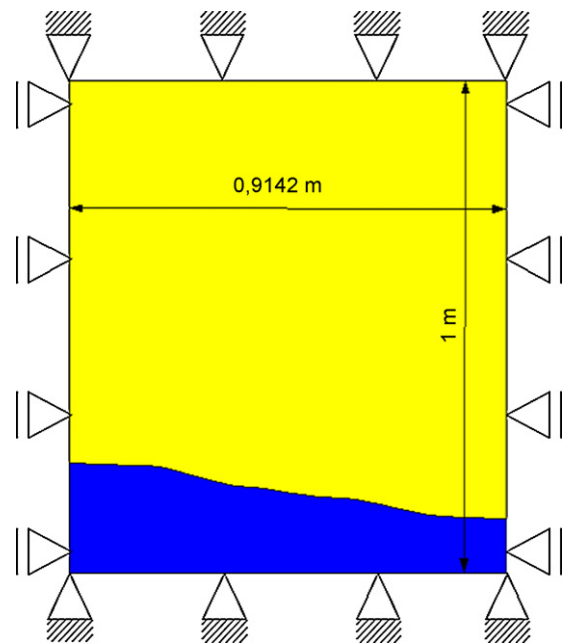

Fig. 9. Schematic view of the boundary conditions for the test case analyzed by van Keken et al. (1997).
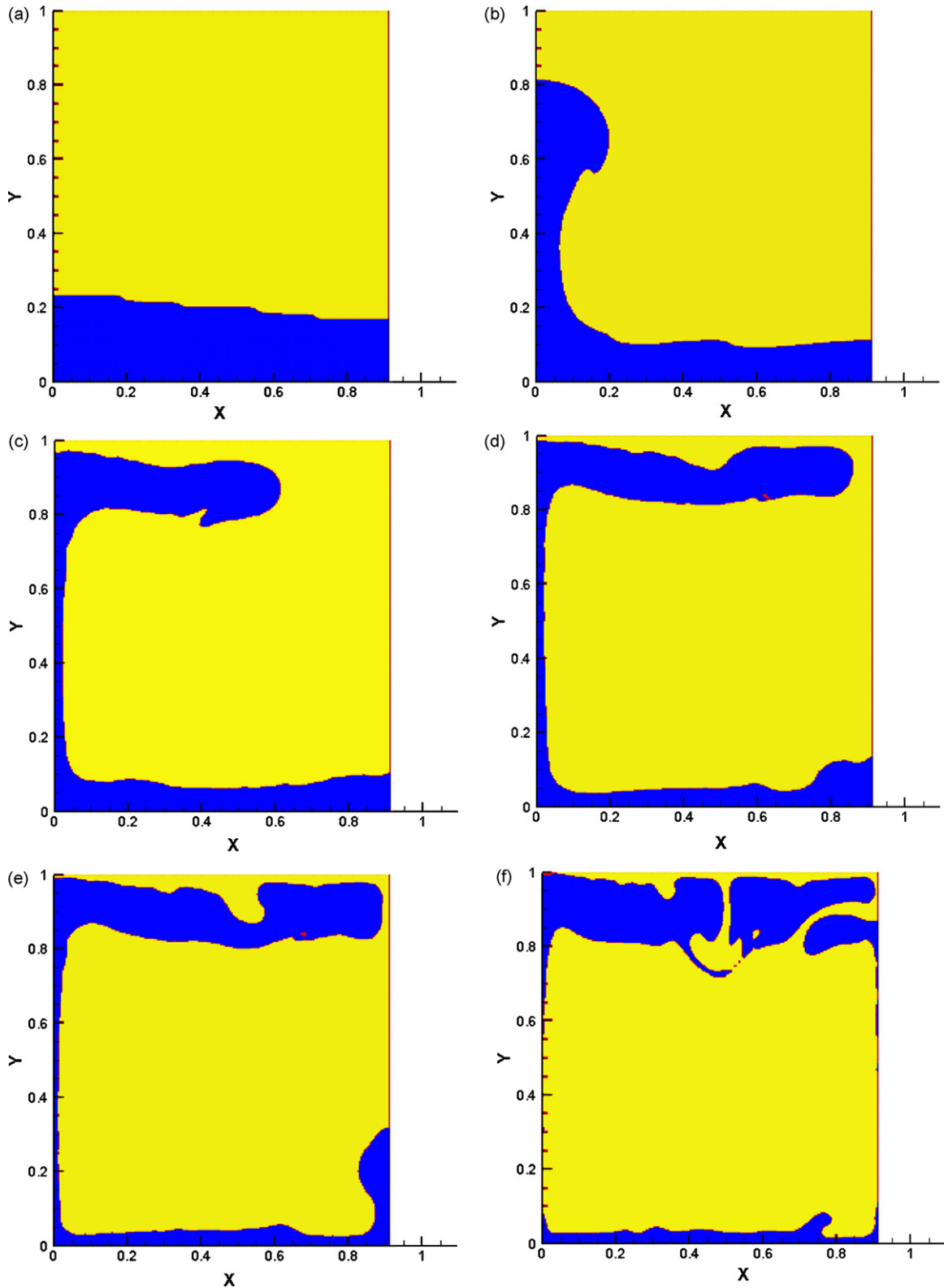
Fig. 10. Validation of the viscous behaviour in the test case proposed by van Keken et al. (1997).

same material in all the domains with the exception of a small block of weaker material centered at the lower part of the model (Fig. 11). The domain is compressed on its left and right sides at a constant velocity of 0.1 cm s^{-1}. Viscosity behaviour was switched off by setting a very high viscosity value. There are no gravity forces in this simulation.

The main properties of the materials that compose the domain can be seen in Table 4. The properties of the weak material are exactly the same as the properties of the stronger one but with a shear elastic modulus (G) two orders of magnitude smaller. The remeshing algorithm was disabled in order to verify that the plastic deformation would concentrate as expected.
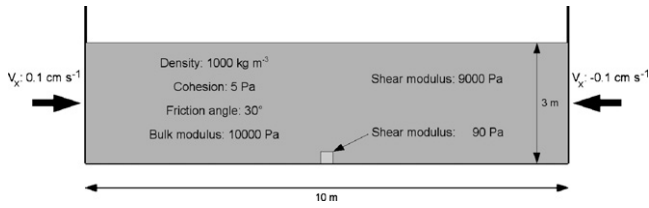
Fig. 11. Model setup for the compression experiment. The domain consists of a homogeneous block with a small intrusion of weaker material centered at the lower boundary. The properties of both materials only differ in the shear modulus. The block is compressed with a velocity of 0.1 cm s^{-1}.

Table 4
Main features of materials present in the compression experiment.

Parameter	Strong material	Weak material
Density, ρ (kg m^{-3})	1,000	1,000
Cohesion, σ_0 (Pa)	5	5
Int. angle friction, ϕ	30°	30°
Bulk modulus, K (Pa)	10,000	10,000
Shear modulus, G (Pa)	9,000	90
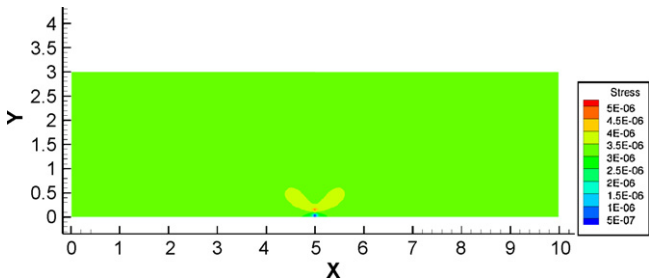
Fig. 12. Stress distribution over the block at $t = 0.8$ s. Plastic yield is reached at this moment.

At the beginning of simulation the body accumulates stress until it reaches the plastic yield (Fig. 12) at approximately 0.8 s. After that, shear bands start to grow from the weak point towards the surface.

The instantaneous strain rate at 10 s is shown in Fig. 13. It can be seen that deformation is mostly concentrated over the two shear bands and that this final configuration is composed of three rigid blocks with almost no internal deformation. The displacements of these blocks can be seen in Fig. 14. There, the vertical velocity is plotted and it is clear that, after the breakup, the uplift of the block in the center part of the domain follows, with no vertical movement on the other two blocks. Also, the accumulated plastic deformation and arrows indicating displacements (Fig. 15) show the formation of these blocks after both shear bands are formed.
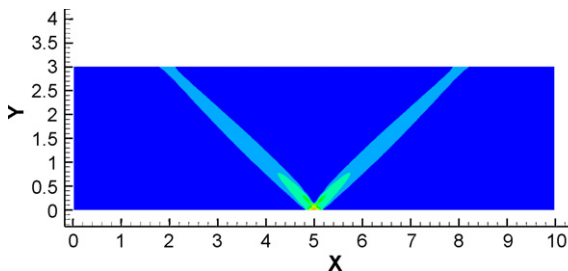

Fig. 13. Instantaneous strain rate at $t = 10$ s. Shear bands are already formed and deformation concentrates there.
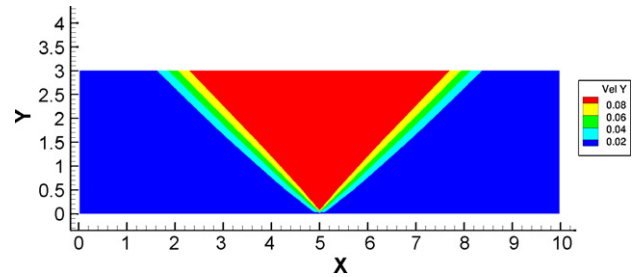

Fig. 14. Displacements over the domain at $t = 10$ s. One can see the three blocks with different motion due to the accommodation of the deformation only on the two *faults* formed from the weaker point.
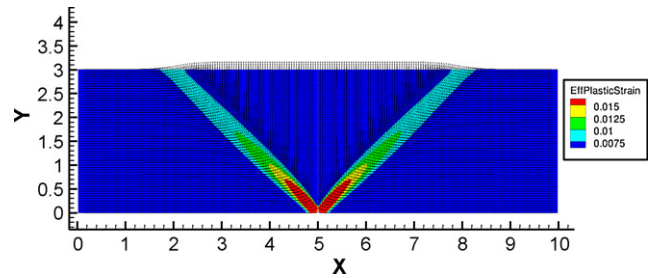

Fig. 15. Accumulated plastic strain and displacements at $t = 10$ s. One can see that the plastic yield is predominantly reached on the two shear bands.

7. Discussion and summary

The coupled thermo-mechanical model presented in this paper is based on deformation of solids and can simulate elasto-visco-plastic behaviour of rocks under different kinematical conditions. Complex non-linear rheology can be defined, including different types of creep (dislocation, diffusion and Peierls).

The implementation relays on an implicit Backward Euler approach, which makes it inherently stable from the time step point of view, compared to the explicit codes, which need shorter time steps. Newton–Raphson iteration, consistent tangential operator (Simo and Taylor, 1985) and the method published by Hughes (1980) for the stress update procedure improve the convergence even under strong non-linear cases.

Two types of elements are included in the code. On one hand, the element published by Liu et al. (1994), has the following features:

- 4 nodes element: requires less computational effort to calculate the solution,
- reduced and selective integration: avoids the volumetric locking and implies a lower computational cost,
- a modified gradient matrix: diminishes the *hourglass* effect caused by the reduced integration.

On the other hand, a standard quadrilateral element with 8 nodes, whose main features are:

- slower iterations due to the increase in definition, but less iterations due to the faster convergence to solution,
- no hourglass modes. Thus, remeshing due to this effect and also the techniques to diminish it are avoided.

Also, a remeshing algorithm based on the Laplace equation was implemented. The position of the nodes belonging to the boundary is imposed as a Dirichlet condition. The translation of the domain state from the distorted mesh to the undistorted one is calculated after remeshing based on the information (stress, material properties) stored by the markers (Lagrangian particles).

The domain can be discretized with a non-uniform mesh, which has the advantage of increasing the resolution on regions of interest. An arbitrary number and distribution of materials can be defined and their properties are parametrized. The different types of behaviour were validated by means of standard test cases. Thus, not only the results are validated, but also the good performance of the remeshing algorithm and the mapping of the state variables between the old and new mesh could be tested by the Rayleigh–Taylor instability test case.

At least two direct solvers were linked to the implementation (Pardiso and MUMPS), which can run in parallel the most time-consuming part of the execution. Pardiso has a very good performance on multi-processor computers with shared memory using extensive use of OpenMP techniques. MUMPS was developed to be scalable when it is used in a cluster environment, using standard Message Passing Interface (MPI) methods. Even if the non-uniform mesh can imply finer resolution on regions of interest, the price to pay is a coarser definition on other parts of the model. Under this assumption and when trying to solve large domains, it is necessary to switch to a full parallel approach. The substructure technique proposed by Bathe (1996) is one of the possibilities that we evaluate. Other option could be a multigrid approach as implemented by Moresi et al. (2003) or something similar to Octree, as implemented by Braun et al. (2008).

A very simple approach to the role of fluid in zones of the domain can be achieved by means of a dynamical manipulation of material properties, which leads to an instant response from the thermo-mechanical implementation. However, its displacement and modification of variables like effective pressure are still not possible at this stage of development. Therefore, we believe that coupled porous flow should be included in our implementation in order to represent this processes in a proper way.

Acknowledgements

References

Amestoy, P.R., Duff, I., L'Excellent, J.Y., 2000. Multifrontal parallel distributed symmetric and unsymmetric solvers. Computer Methods in Applied Mechanics and Engineering 184, 501–520.

Babeyko, A.Y., Sobolev, S.V., Trumbull, R.B., Oncken, O., Lavier, L.L., 2002. Numerical models of crustal scale convection and partial melting beneath the Altiplano - Puna plateau. Earth and Planetary Science Letters 199 (373), 388.

Babeyko, A.Y., Sobolev, S.V., Vietor, T., Oncken, O., Trumbull, R.B. 2006. Numerical study of weakening processes in the Central Andean back-arc. In: Oncken, O., Chong, G., Franz, G., Giese, P., Goetze, H.-J., Ramos, V.A., Strecker, M.R., Wigger, P. (Eds.), The Andes - Active Subduction Orogeny. Springer-Verlag, 569 pp. (chapter 24).

Bathe, K.-J., 1996. Finite Element Procedures. Prentice Hall, New Jersey.

Blackford, L.S., Choi, J., Cleary, A., D'Azevedo, E., Demmel, J., Dhillon, I., Dongarra, J., Hammarling, S., Henry, G., Petitet, A., Stanley, K., Walker, D., Whaley, R.C., 1997. ScaLAPACK Users' Guide. Society for Industrial and Applied Mathematics, Philadelphia, PA, ISBN 0-89871-397-8 (paperback).

Braun, J., Thieulot, C., Fullsack, P., DeKool, M., Beaumont, C., Huismans, R., 2008. DOUAR: a new three-dimensional creeping flow numerical model for the solution of geological problems. Physics of the Earth Interiors 171, 76–91.

Byerlee, J., 1978. Friction of rocks. Pure and Applied Geophysics 116, 615–626.

Carey, G.F., Oden, J.T., 1984. Finite elements – computational aspects, vol. III, first edition. Prentice-Hall, Inc., New Jersey.

Cristallini, E.O., Allmendinger, R.W., 2001. Pseudo 3-D modeling of trishear fault-propagation folding. Journal of Structural Geology 23, 1883–1899.

Dongarra, J., 2002. Basic linear algebra subprograms technical forum standard. International Journal of High Performance Applications and Supercomputing 16 (2), 115–199.

Fullsack, P., 1995. An arbitrary Lagrangian-Eulerian formulation for creeping flows and its application in tectonic models. Geophysics Journal International 120, 1–23.

Gerya, T.V., Yuen, D.A., 2003. Characteristics-based marker-in-cell method with conservative finite-differences schemes for modeling geological flows with strongly variable transport properties. Physics of the Earth Interiors 140, 293–318.

Gerya, T.V., Yuen, D.A., 2007. Robust characteristics method for modeling multiphase visco-elasto-plastic thermo-mechanical problems. Physics of the Earth Interiors 163, 83–205.

Harlow, F.H., Welch, J.E., 1965. Numerical calculation of time-dependent viscous incompressible flow of fluid with free surface. The Physics of Fluids 8 (12), 2182–2189.

Hughes, T.J.R., 1980. Generalization of selective integration procedures to anisotropic and nonlinear media. International Journal for Numerical Methods for Engineering 15, 1413–1418.

Hughes, T.J.R., Winget, J., 1980. Finite rotation effects in numerical integration of rate constitutive equations arising in large-deformation analysis. International Journal for Numerical Methods for Engineering 15, 1862–1867.

Jaoul, O., Tullis, J., Kronenberg, A., 1984. The effect of varying water contents on the creep behavior of heavytree quartzite. Journal of Geophysical Research 89 (B6), 4298–4312.

Kameyama, M., Yuen, D.A., Karato, S.I., 1999. Thermal-mechanical effects on low-temperature plasticity (the Peierls mechanism) on the deformation of a viscoelastic shear zone. Earth and Planetary Science Letters 168, 159–172.

Karypis, G., Kumar, V., 1999. A fast and high quality multilevel scheme for partitioning irregular graphs. SIAM Journal on Scientific Computing 20 (1), 359–392.

Liu, W.K., Hu, Y.-K., Belytschko, T., 1994. Multiple Quadrature underintegrated finite elements. International Journal for Numerical Methods in Engineering 37, 3263–3289.

Mackwell, S.J., Zimmerman, M.E., Kohlstedt, D.L., 1998. High temperature deformation of dry diabase with application to tectonics on Venus. Journal of Geophysical Research 103 (B1), 975–984.

Moresi, L.N., Dufour, F., Muhlhaus, H.B., 2003. A Lagrangian integration point finite element method for large deformation modeling of viscoelastic geomaterials. Journal of Computational Physics 184, 476–497.

Novoselov, R.Y., Lawrence, D.A., Pao, L.Y., 2002. Haptic rendering of data on unstructured tetrahedral grids. International Symposium on Haptic Interfaces for Virtual Environment and Teleoperator Systems. In: IEEE Computer Society, Los Alamitos, CA, USA, pp. 193–200.

Petrunin, A., Sobolev, S.V., 2006. What controls thickness of sediments and lithospheric deformation at a pull-apart basin? Geology 34, 389–392.

Popov, A.A., Sobolev, S.V., 2008. Slim3d: a tool for three-dimensional thermomechanical modeling of the lithospheric deformation with elasto-viscoplastic rheology. Physics of the Earth Interiors 171, 55–75. doi:10.1016/j.pepi.2008.03.007.

Pysklywec, R.N., 2001. Evolution of subducting mantle lithosphere at a continental plate boundary. Geophysical Research Letters 28 (23), 4399–4402.

Pysklywec, R.N., Beaumont, C., 2004. Intraplate tectonics: feedback between radioactive thermal weakening and crustal deformation driven by mantle lithosphere instabilities. Earth and Planetary Science Letters 221, 275–292.

Quinteros, J., Jacovkis, P.M., Ramos, V.A., 2006. Evolution of the upper crustal deformation in subduction zones. Journal of Applied Mechanics 73, 984–994.

Quinteros, J., Jacovkis, P.M., Ramos, V.A., 2007. Diseño flexible y modular de modelos numéricos basados en elementos finitos. In: Elaskar, S.A., Pilotta, E.A., Torres, G.A. (Eds.), Mecánica Computacional, vol. XXVI, Córdoba, Argentina, pp. 1724–1740. Asociacióon Argentina de Mecánica Computacional.

Schenk, O., Gaertner, K., Fichtner, W., Stricker, A., 2001. Pardiso: a highperformance serial and parallel sparse linear solver in semiconductor device simulation. Future Generation Computer Systems 18, 69–78.

Simo, J.C., Taylor, R.L., 1985. Consistent tangent operators for rate-independent elasto-plasticity. Computer Methods in Applied Mechanics and Engineering 48, 101–118.

Sobolev, S.V., Babeyko, A.Y., 2005. What drives orogeny in the Andes? Geology 33, 617–620.

Strayer, L.M., Suppe, J., 2002. Out-of-plane motion of a thrust sheet during along-strike propagation of a thrust ramp: a distinct-element approach. Journal of Structural Geology 24, 637–650.

van Keken, P.E., King, S.D., Schmeling, H., Christensen, U.R., Neumeister, D., Doin, M.P., 1997. A comparison of methods for the modeling of thermo-chemical convection. Journal of Geophysical Research 102, 22477–22495.

Willett, S.D., 1999. Orogeny and orography: the effects of erosion on the structure of mountain belts. Journal of Geophysical Research 104 (B12), 28957–28981.